Statistical characteristics of wall turbulence with a passive scalar

By Y. NAGANO and M. TAGAWA

Department of Mechanical Engineering, Nagoya Institute of Technology, Gokiso-cho, Showa-ku, Nagoya 466, Japan

Various types of moments of velocity and scalar fluctuations of the first to the fourth order have been measured and analysed. First, an orthogonal series expansion for the three-dimensional joint probability density function (p.d.f.) is developed using the cumulants and Hermite polynomials. This p.d.f. is found to provide satisfactory predictions for the statistical characteristics, including triple products, of turbulent momentum and scalar transfer. Next, the conditional sampling and averaging technique is employed to investigate the statistical characteristics of coherent turbulent transfer processes of momentum and scalar. Conditional p.d.f.s are developed for various moments of velocity and scalar up to the third order. It is shown that the present p.d.f.s can predict the detailed role of coherent motions in the dynamics of wall turbulent shear flows and in the relevant process of scalar transport by turbulence. In particular, the importance of coherent motions in the turbulent diffusion process of Reynolds-stress components and scalar fluxes is demonstrated for the first time by the present theory.

1. Introduction

Transfer problems of momentum and scalar have begun to be analysed using recent advanced turbulence models such as those based on Reynolds-stress and scalar-flux closures (Elghobashi & Launder 1981). Results, however, are not as satisfactory as initially expected, mainly owing to a few unreasonable hypotheses in the models (Lumley 1978). In order to resolve pertinent problems adequately, we need correct knowledge of the statistical characteristics of the first- and second-order moments of velocity and scalar fluctuations, and the relevant processes of turbulent diffusion (i.e. third-order moments), all of which are basic parameters in the stress and scalar flux equation models.

Antonia & Atkinson (1973) first investigated statistical characteristics of Reynolds shear stress without the aid of the assumption of Gaussian behaviour. Their approaches, however, cannot be applied to the analysis of turbulent scalar transfer and third-order moments of velocity and scalar, since the derived probability density function (p.d.f.) is only valid for second-order moments in a velocity field without passive contaminants. Furthermore, in the analysis of third-order moments, we cannot generally use the conventional assumption of Gaussian behaviour because of the essential unreality according to which a mean value is consistently zero.

On the other hand, it is now widely known that the coherent structures exist spatially and temporally in the near-wall region, and dominate the fluid-dynamical characteristics of wall turbulence. Various features of the coherent structures have been investigated in detail, particularly since the discovery of the prominent role of

coherent motions in the generation mechanism of turbulence kinetic energy. For example, Lu & Willmarth (1973) and Hishida & Nagano (1981), using a uv-quadrant analysis, have revealed that most of the Reynolds shear stress uv is produced by ejection- and sweep-type motions (essential elements of coherent structures).

During the past decade, we have investigated the mechanism of transport phenomena in turbulence from various viewpoints to correlate the transfer processes of momentum and scalar with these coherent fluid motions (Hishida & Nagano 1979; Nagano & Hishida 1985; Hishida, Nagano & Tagawa 1986; Nagano & Tagawa 1988). However, there is not yet a full explanation of the problems of how or how strongly these organized fluid motions dominate the statistical characteristics of scalar turbulence, e.g. scalar-fluctuation variance, turbulent scalar fluxes and triple correlations between velocity and scalar.

Perry & Hoffmann (1976) examined the similarity between the Reynolds shear stress uv and turbulent scalar flux $v\theta$ from the results of a conditional analysis for a heated flat-plate boundary-layer flow. In their experimental study using quadrant analysis, however, the Reynolds shear stress uv was analysed in the (u, v)-plane and the turbulent scalar flux $v\theta$ in the (v, θ)-plane. Hence, the correspondence between scalar transport and fluid motions was not strictly specified.

The present study has three objectives: (i) to obtain experimental evidence of high-order moments related to turbulent momentum and scalar transfer in a wall turbulent shear flow; (ii) to develop a theory by which the principal statistical aspects of these moments can be predicted; and (iii) to identify the role of coherent structures in transport phenomena from a statistical viewpoint. The structural knowledge of turbulent momentum and scalar transfer obtained previously is reflected in the present statistical investigation. In the theory, we have used the cumulant-discard method (Monin & Yaglom 1971) to take into account a departure from Gaussian behaviour (Kampé de Fériet 1966; Frenkiel & Klebanoff 1967; Sullivan & Yip 1985). Then we have developed multidimensional joint p.d.f.s for quantities controlling transport phenomena. The present theory covers completely the reported two-dimensional probability theory (Antonia & Atkinson 1973; Nakagawa & Nezu 1977). The validity of the theory has been verified by application to the prediction of experimental results of p.d.f. distributions of higher-order moments. Particular attention is directed to the study of statistical characteristics of third-order moments, because measurements of their p.d.f. distributions are few and current modelling is quite *ad hoc*. In the latter half of this paper, we have expanded the theoretical treatment for the three-dimensional joint p.d.f. by combining it with a conditional-sampling technique, and investigated the internal structures of velocity and scalar fluctuations, Reynolds shear stress, turbulent scalar fluxes, and turbulent diffusion, i.e. the triple products of velocity and scalar. The organized motions and their contributions to transport process in wall turbulence are discussed in concrete terms.

2. Experimental facility and data acquisition

The experimental apparatus used for the present study is the same as that described by Hishida & Nagano (1979). The experiment was performed in an air flow in a 45.68 mm ID reamed brass tube heated to a uniform wall temperature of 100 °C at a Reynolds number (based on bulk velocity and pipe diameter) of 40000. Both velocity and thermal fields were fully developed at the measurement locations. The centreline velocity $\bar{U}_c$ and temperature $\bar{\Theta}_c$ were 17.2 m/s and 41.2 °C, respectively.

Fluctuations of velocity components, u (axial) and v (normal), and scalar (temperature), θ, were simultaneously measured with a specially devised three-wire probe. The probe consisted of two hot wires, one a symmetrically bent V-shaped wire (Nagano & Hishida 1985; Hishida *et al.* 1986) and the other a single straight one, together with a cold wire (Hishida & Nagano 1978). It should be noted that the probe was constructed as small as practicable in order to assure spatial resolution without causing any thermal and aerodynamic interference between each wire, i.e. the sensing part was kept smaller than 22 viscous units or 6η (where η is the Kolmogorov microscale). All data were recorded in analog form with an FM data recorder (TEAC R-210B) and then reproduced for conversion to digital form. The digitized data were stored on magnetic tape with a 12 bit analog-to-digital converter (TEAC DR-2000). For each set of u-, v- and θ-fluctuations, the real-time sampling frequency was 32 kHz, and the number of data points per measurement was 65536. The statistical analysis of the data was performed on a FACOM M-382 computer system.

3. Basic theory

To analyse generally the statistics of momentum and scalar transfer, we should introduce the four-dimensional joint p.d.f. with three components of a velocity vector $V(u, v, w)$ and a fluctuating scalar θ as random variables. In two-dimensional turbulent flows, however, the random properties pertaining to transport processes can be sufficiently specified by the three-dimensional joint p.d.f. $P(u, v, \theta)$. When a Gaussian distribution is supposed to be $P(u, v, \theta)$, mean values of any third-order moments are consistently zero, which is usually not the case in an actual phenomenon. Thus, as given below, we have developed a more general representation for $P(\hat{u}, \hat{v}, \hat{\theta})$ using the characteristic function ψ, which is the Fourier transform of the p.d.f. In what follows, a circumflex denotes the normalization by the respective r.m.s. value, and an overbar represents an expected value or time average.

$$\psi(\xi, \eta, \zeta) = \iiint_{-\infty}^{\infty} P(\hat{u}, \hat{v}, \hat{\theta}) \, \exp\{i(\hat{u}\xi + \hat{v}\eta + \hat{\theta}\zeta)\} \, d\hat{u} \, d\hat{v} \, d\hat{\theta}. \tag{1}$$

If a particular form is given to the characteristic function ψ defined by (1), $P(\hat{u}, \hat{v}, \hat{\theta})$ can be obtained by executing the inverse Fourier transform of ψ. Two expressions for ψ are conceivable.

(*A*) Description of ψ in terms of a moment m_{pqr}. The following relation holds between m_{pqr} and ψ:

$$\left. \frac{\partial^K \psi(\xi, \eta, \zeta)}{\partial \xi^p \, \partial \eta^q \, \partial \zeta^r} \right|_{\xi=\eta=\zeta=0} = i^K m_{pqr}, \tag{2}$$

where $K = p + q + r$ and

$$m_{pqr} = \overline{\hat{u}^p \hat{v}^q \hat{\theta}^r}$$

$$= \iiint_{-\infty}^{\infty} \hat{u}^p \hat{v}^q \hat{\theta}^r \, P(\hat{u}, \hat{v}, \hat{\theta}) \, d\hat{u} \, d\hat{v} \, d\hat{\theta}. \tag{3}$$

Thus, we obtain the following expression for ψ:

$$\psi(\xi, \eta, \zeta) = \sum_{p,q,r=0}^{\infty} \frac{i^K}{p! \, q! \, r!} m_{pqr} \xi^p \eta^q \zeta^r. \tag{4}$$

(B) Description of ψ in terms of a cumulant k_{pqr}. The definition of the cumulant k_{pqr} is

$$\frac{\partial^K \ln \psi (\xi, \eta, \zeta)}{\partial \xi^p \partial \eta^q \partial \zeta^r}\bigg|_{\xi=\eta=\zeta=0} = i^K k_{pqr}. \tag{5}$$

Thus,
$$\psi(\xi, \eta, \zeta) = \exp\left(\sum_{p,q,r=0}^{\infty} \frac{i^K}{p!\,q!\,r!} k_{pqr} \xi^p \eta^q \zeta^r\right). \tag{6}$$

The relations between m_{pqr} and k_{pqr} are

$$\left.\begin{aligned}
&m_{000} = 1, \quad k_{000} = 0 \quad \text{for } K = 0;\\
&m_{pqr} = k_{pqr} \quad \text{for } 1 \leqslant K \leqslant 3;\\
&\text{and}\\
&m_{400} = k_{400}+3, \quad m_{040} = k_{040}+3, \quad m_{004} = k_{004}+3,\\
&\left.\begin{aligned}
&m_{310} = k_{310}+3m_{110}, \quad m_{301} = k_{301}+3m_{101}, \quad \ldots, \quad m_{013} = k_{013}+3m_{011}\\
&m_{220} = k_{220}+2(m_{110})^2+1, \quad \ldots, \quad m_{112} = k_{112}+2m_{101}m_{011}+m_{110}.
\end{aligned}\right\} \quad \text{for } K = 4.
\end{aligned}\right\}$$
$$\tag{7}$$

Similarly, the relations for $K \geqslant 5$ can be deduced, but the calculations become increasingly cumbersome.

Now, the Gaussian joint p.d.f. can be written as

$$P_G(\hat{u}, \hat{v}, \hat{\theta}) = \frac{\exp\left\{-\left(\sum_{i,j=1}^{3} \Delta_{ij} \hat{\chi}_i \hat{\chi}_j\right)\Big/(2|\boldsymbol{R}|)\right\}}{(2\pi)^{\frac{3}{2}} |\boldsymbol{R}|^{\frac{1}{2}}}, \tag{8}$$

with $\hat{\chi}_1 = \hat{u}$, $\hat{\chi}_2 = \hat{v}$ and $\hat{\chi}_3 = \hat{\theta}$, where

$$\boldsymbol{R} = \begin{pmatrix} 1 & R_{12} & R_{13} \\ R_{12} & 1 & R_{23} \\ R_{13} & R_{23} & 1 \end{pmatrix}; \quad \Delta_{ij} \text{ is the cofactor of the matrix } \boldsymbol{R};$$

and R_{ij} denotes the correlation coefficient between χ_i and $\chi_j (= \overline{\hat{\chi}_i \hat{\chi}_j})$. In a Gaussian field given by (8), moments and cumulants preserve the following characteristics:

(a) odd-order moments (i.e. K is odd) are all zero;

(b) even-order moments (i.e. K is even) can be represented by zero- and second-order moments;

(c) for $K \geqslant 3$, all cumulants are zero.

In a statistical analysis of a field close to Gaussian, (c) is quite useful. It is generally recognized that probability distributions of turbulent phenomena do not deviate largely from a Gaussian distribution. Hence, adopting (B) for describing ψ and using the characteristic (c), we can accurately represent the p.d.f. $P(\hat{u}, \hat{v}, \hat{\theta})$ with a small number of series-expansion terms. From (6) and (7), we obtain

$$\psi(\xi, \eta, \zeta) = \exp\left\{-\tfrac{1}{2}(\xi^2+\eta^2+\zeta^2+2R_{uv}\xi\eta+2R_{u\theta}\xi\zeta+2R_{v\theta}\eta\zeta)\right.$$
$$\left. + \sum_{K \geqslant 3}^{\infty} \frac{i^K}{p!\,q!\,r!} k_{pqr} \xi^p \eta^q \zeta^r\right\}, \tag{9}$$

where $k_{110} = m_{110} = \overline{\hat{u}\hat{v}} = R_{uv}$, $k_{101} = R_{u\theta}$ and $k_{011} = R_{v\theta}$. Equation (9) can be rewritten in either of two ways:

$$\psi(\xi, \eta, \zeta) = \exp\{-\tfrac{1}{2}(\xi^2+\eta^2+\zeta^2)\} \sum_{p,q,r=0}^{\infty} C_{pqr} i^K \xi^p \eta^q \zeta^r; \tag{10}$$

$$\psi(\xi, \eta, \zeta) = \exp\{-\tfrac{1}{2}(\xi^2 + \eta^2 + \zeta^2 + 2R_{uv}\xi\eta + 2R_{u\theta}\xi\zeta + 2R_{v\theta}\eta\zeta)\}$$

$$\times \sum_{p,q,r=0}^{\infty} D_{pqr} i^K \xi^p \eta^q \zeta^r, \quad (11)$$

where C_{pqr} and D_{pqr} are the coefficients in the power-series expansion of (9). If we use (10), the final form for $P(\hat{u}, \hat{v}, \hat{\theta})$ is expressed by the products of one-dimensional Hermite polynomials. On the other hand, with (11), $P(\hat{u}, \hat{v}, \hat{\theta})$ is represented by three-dimensional conjugate Hermite polynomials. The study by Antonia & Atkinson (1973) on a two-dimensional p.d.f. with two random variables showed that an expression with conjugate Hermite polynomials predicted the experimental results a little better than one with one-dimensional Hermite polynomials. However, even in their two-dimensional analysis, numerous series-expansion terms were needed for the p.d.f. and the expression was complex. Since, in the present study, we analyse the third-order moments in a three-dimensional field, the use of (11) will obviously make mathematical treatment extremely difficult. In addition, to apply a p.d.f. to multisided analyses of transport processes of momentum and scalar and to modelling third-order moments, it is desirable to keep the number of parameters as few as possible. Hence, we adopt expression (10).

Substituting the characteristic function (10) into (1) and performing the inverse Fourier transform, we obtain the following general representation for $P(\hat{u}, \hat{v}, \hat{\theta})$:

$$P(\hat{u}, \hat{v}, \hat{\theta}) = \frac{1}{(2\pi)^3} \iiint_{-\infty}^{\infty} \psi(\xi, \eta, \zeta) \exp\{-i(\hat{u}\xi + \hat{v}\eta + \hat{\theta}\zeta)\} \, d\xi \, d\eta \, d\zeta$$

$$= \frac{1}{(2\pi)^{\frac{3}{2}}} \sum_{p,q,r=0}^{\infty} C_{pqr} H_p(\hat{u}) H_q(\hat{v}) H_r(\hat{\theta}) \exp\{-\tfrac{1}{2}(\hat{u}^2 + \hat{v}^2 + \hat{\theta}^2)\}, \quad (12)$$

where

$$H_n(\chi) = (-1)^n \exp(\tfrac{1}{2}\chi^2) \frac{d^n}{d\chi^n} \exp(-\tfrac{1}{2}\chi^2). \quad (13)$$

$H_n(\chi)$ is an Hermite polynomial. The subsequent analysis has been made for $K \leqslant 4$. Calculating C_{pqr} from (9) and (10) yields

$$\left.\begin{aligned}
&C_{000} = 1, \quad C_{100} = C_{010} = C_{001} = 0, \quad C_{200} = C_{020} = C_{002} = 0, \\
&C_{110} = R_{uv}, \quad C_{101} = R_{u\theta}, \quad C_{011} = R_{v\theta}, \quad C_{300} = \tfrac{1}{6}k_{300}, \quad C_{030} = \tfrac{1}{6}k_{030}, \quad \dots, \\
&C_{210} = \tfrac{1}{2}k_{210}, \quad \dots, \quad C_{012} = \tfrac{1}{2}k_{012}, \quad C_{111} = k_{111}, \\
&C_{400} = \tfrac{1}{24}k_{400}, \quad \dots, \quad C_{310} = \tfrac{1}{6}k_{310}, \quad \dots, \quad C_{013} = \tfrac{1}{6}k_{013}, \\
&C_{220} = \tfrac{1}{4}(k_{220} + 2R_{uv}^2), \quad C_{202} = \tfrac{1}{4}(k_{202} + 2R_{u\theta}^2), \quad \dots, \quad C_{112} = \tfrac{1}{2}(k_{112} + 2R_{u\theta}R_{v\theta}).
\end{aligned}\right\} \quad (14)$$

The coefficients listed above are determined from the measured correlations up to the fourth order (see (7)).

4. High-order moments and probability distributions of velocity and scalar

4.1. *Probability density distributions of velocity and scalar fluctuations*

The p.d.f. distributions $P(\hat{v})$ and $P(\hat{\theta})$ at various locations, from within the sublayer out to the pipe centreline ($y^+ = 863.0$, y^+ being dimensionless distance from the wall $= u_\tau y/\nu$), are shown in figure 1. The solid lines indicate the theoretical values derived from (12), and the broken lines represent the Gaussian distributions. Thus,
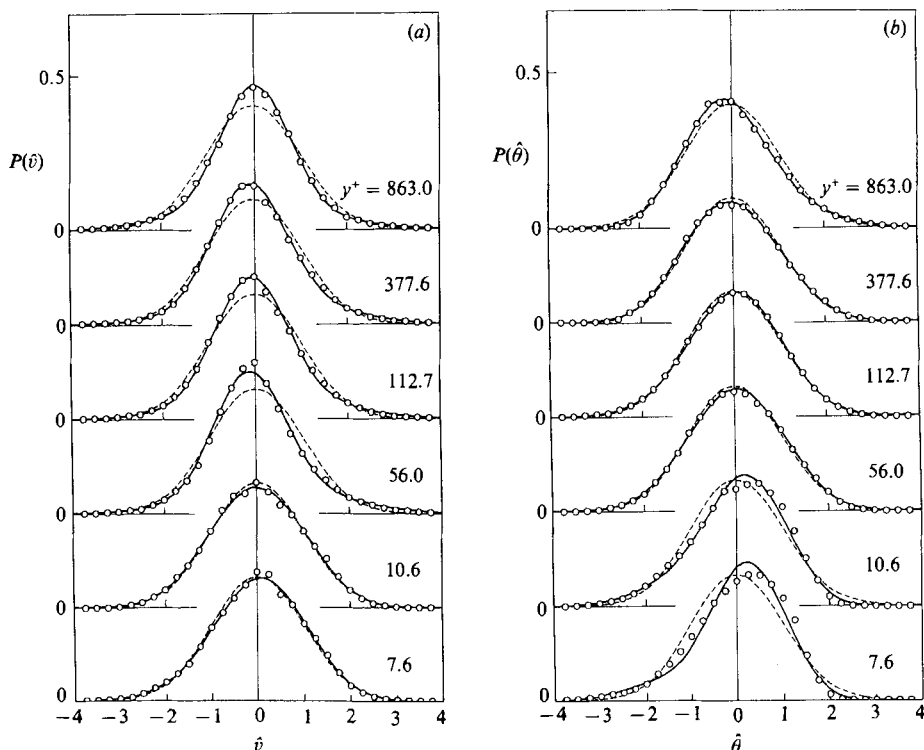
FIGURE 1. Probability density distributions of velocity and scalar fluctuations. (a) $P(\hat{v})$: O, experiment; ——, equation 15(a); ———, Gaussian. (b) $P(\hat{\theta})$: O, experiment; ——, equation 15(b); ———, Gaussian.

the theoretical values of $P(\hat{v}), P(\hat{\theta})$ and the first-order Gaussian p.d.f. $P_G(\chi)$ are given by

$$P(\hat{v}) = \iint_{-\infty}^{\infty} P(\hat{u}, \hat{v}, \hat{\theta}) \, d\hat{u} \, d\hat{\theta}$$

$$= P_G(\hat{v}) \{1 + C_{030}(\hat{v}^3 - 3\hat{v}) + C_{040}(\hat{v}^4 - 6\hat{v}^2 + 3)\}, \tag{15a}$$

$$P(\hat{\theta}) = P_G(\hat{\theta}) \{1 + C_{003}(\hat{\theta}^3 - 3\hat{\theta}) + C_{004}(\hat{\theta}^4 - 6\hat{\theta}^2 + 3)\}, \tag{15b}$$

$$P_G(\chi) = \exp(-\tfrac{1}{2}\chi^2)/(2\pi)^{\frac{1}{2}}, \quad \chi = \hat{v} \quad \text{or} \quad \hat{\theta}. \tag{16}$$

The $P(\hat{v})$-curve is very close to Gaussian near the wall. A departure from the Gaussian distribution, however, occurs in the log-law region and in the core region of the flow. The $P(\hat{\theta})$-curve, on the other hand, is strongly skewed to the negative side of θ very near the wall, although it may be approximated with a Gaussian distribution in the log-law region. Inversely, $P(\hat{u})$ is skewed positively in the near-wall region (not shown). The measurement of a joint p.d.f. $P(\hat{u}, \hat{v})$ shown in figure 2(a) indicates that the sweep-type motions, rushing into the near-wall region from regions away from the wall, predominate in the near-wall structure, i.e. the large-amplitude motions with u positive and v negative occur most frequently near the wall. The negatively skewed $P(\hat{\theta})$- and positively skewed $P(\hat{u})$-distributions are the consequence of these inrushes of low-enthalpy and high-momentum fluid. Totally opposite trends are
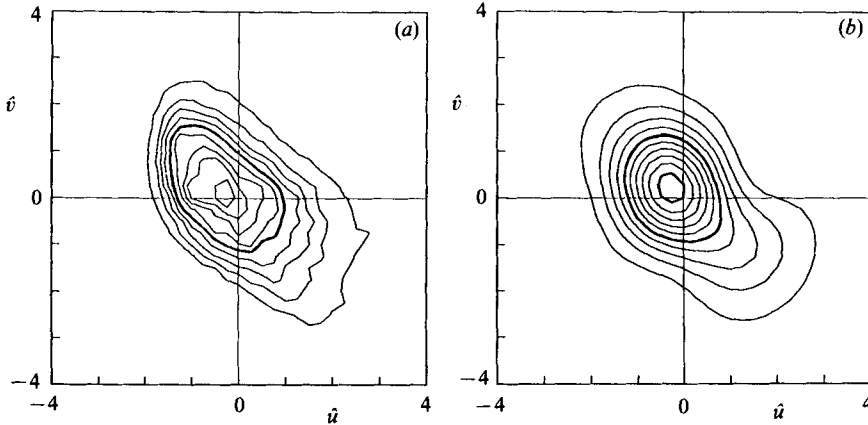
FIGURE 2. Joint probability density of $\hat{u}$ and $\hat{v}$ ($y^+ = 7.6$). Lines are isocontours with an equal increment of 0.02. (*a*) Experiment; (*b*) prediction.

observed in the core region, reflecting the dominant influence of high-enthalpy and low-momentum fluid ejections from the wall region (Nagano & Tagawa 1988). These unique features, as seen from figure 1, are almost perfectly predicted by (15).

The theoretical value of $P(\hat{u}, \hat{v})$ derived from (12) becomes

$$P(\hat{u}, \hat{v}) = \int_{-\infty}^{\infty} P(\hat{u}, \hat{v}, \hat{\theta}) \, \mathrm{d}\hat{\theta}$$

$$= \frac{1}{2\pi} \sum_{p, q=0}^{K \leqslant 4} C_{pq0} H_p(\hat{u}) H_q(\hat{v}) \exp\{-\tfrac{1}{2}(\hat{u}^2 + \hat{v}^2)\}. \tag{17}$$

Comparison of predictions (figure 2*b*) with measurements (figure 2*a*) proves that (17) represents accurately a highly anisotropic velocity field near the wall. Equation (17) is also identical to the theoretical formula developed by Antonia & Atkinson (1973).

The shapes of p.d.f.s $P(\chi)$ are well marked by the skewness $S(\chi) = \overline{\hat{\chi}^3}$ and the flatness factor $F(\chi) = \overline{\hat{\chi}^4}$. The former is particularly indicative of the probabilistic asymmetry of χ and the latter is a measure of symmetrical peakedness of the probability. A random variable with a Gaussian p.d.f. has values of $S(\chi) = 0$ and $F(\chi) = 3$. The skewness and flatness factors of u-, v- and θ-fluctuations are shown in figures 3 and 4, respectively. The skewness factor $S(u)$ becomes negative in the outer region and positive in the near-wall region, while it is approximately zero over the fully turbulent log region. It is conceivable that a marked change in $S(u)$ for $y^+ < 20$ is a reflection of the existence of coherent motions near the wall. Measurements of $S(u)$ and $S(\theta)$ indicate that u- and θ-fluctuations are skewed in the opposite direction. In contrast, $S(v)$ is essentially positive over most of the pipe section.

Next, we show that the skewness factor is related closely to the fraction of time during which a random variable χ is positive (γ_+) or negative (γ_-). With (15), the time fraction $\gamma_\pm$ is expressed as

$$\gamma_\pm(\chi) = \int_0^\infty P(\pm \hat{\chi}) \, \mathrm{d}\hat{\chi}$$

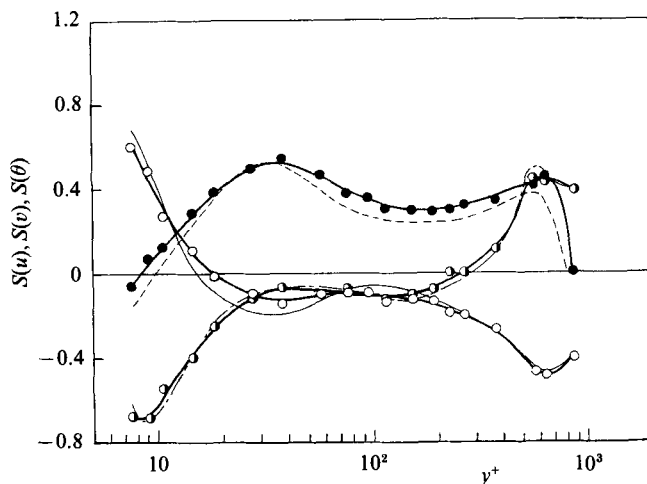$$= \{(\tfrac{1}{2}\pi)^{\frac{1}{2}} \mp \tfrac{1}{6} S(\chi)\}/(2\pi)^{\frac{1}{2}}. \tag{18}$$

FIGURE 3. Skewness factors. Experiments: —O—, $S(u)$; —●—, $S(v)$; —◐—, $S(\theta)$. Calculations from equation (19): ——, $S(u)$; - - -, $S(v)$; —·—, $S(\theta)$.
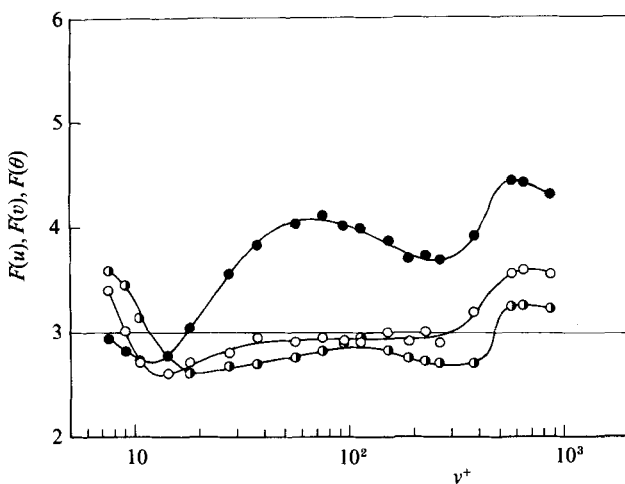

FIGURE 4. Flatness factors. —O—, $F(u)$; —●—, $F(v)$; —◐—, $F(\theta)$.

Thus, (18) gives the following formula for $S(\chi)$:

$$S(\chi) = 3(2\pi)^{\frac{1}{2}}\{\gamma_-(\chi)-\gamma_+(\chi)\}. \tag{19}$$

The values of $S(\chi)$ from (19), calculated using measurements of the time fractions, are compared with the present direct measurements of skewness factors in figure 3. Agreement is seen to be almost perfect, which is important because it demonstrates that the skewness factor characterizing turbulence structures can be represented by the time fractions (i.e. intermittency factor) occupied by positive or negative events of a turbulence component.

The flatness factors $F(u)$ and $F(\theta)$ present similar distributions which are very close to the Gaussian value of 3 in the log-law region. And the skewness factors of u and θ are nearly equal to zero in this region. Thus, the assumption of the Gaussian for $P(\hat{u})$- and $P(\hat{\theta})$-distributions does not lead to a noticeable error, as is shown in
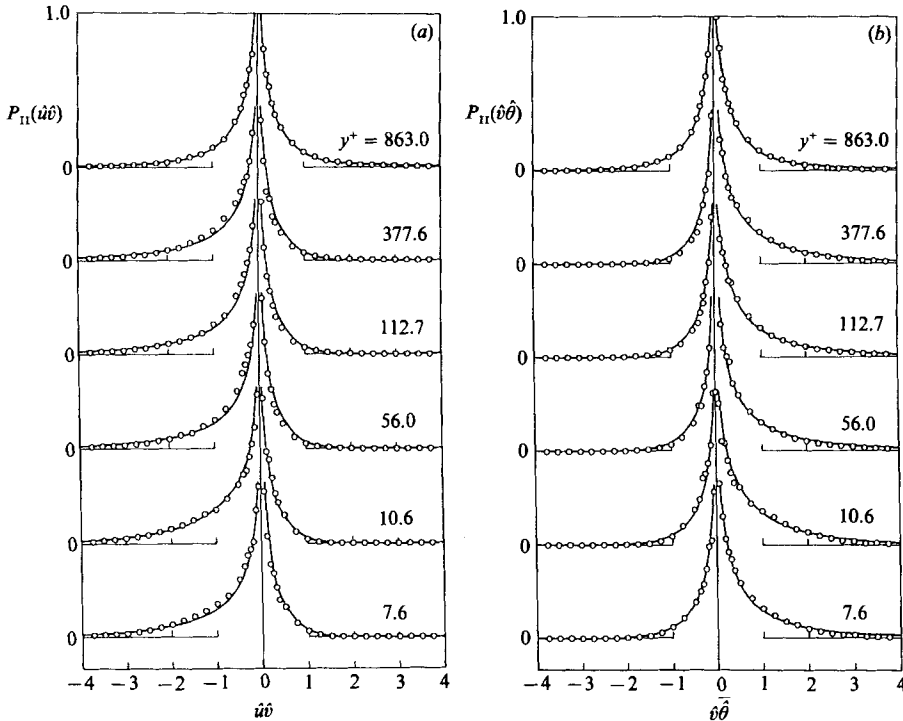
FIGURE 5. Probability density distributions of Reynolds shear stress and turbulent scalar flux. (a) $P_{II}(\hat{u}\hat{v})$: $\bigcirc$, experiment; ———, equation (23). (b) $P_{II}(\hat{v}\hat{\theta})$: $\bigcirc$, experiment; ———, equation (22).

figure 1. Besides, $F(\theta)$ becomes minimum at a location where scalar variance attains a maximum (Hishida *et al.* 1986), which has a close similarity to $F(u)$ behaviour (Zarić 1979). Values of $F(v)$, on the other hand, deviate considerably from the Gaussian value over a greater part of the pipe section (see figure 1).

A full knowledge of skewness and flatness factors near the wall is also required to investigate the coherent structures of wall turbulence. However, we can find few reliable measurements in the literature of these factors (Zarić 1979), particularly for v and θ, so more accurate data are needed. The present distributions of $S(u)$ and $F(u)$ agree quite well with the recent measurements in a flat-plate boundary layer (Durst, Jovanovic & Kanevce 1987).

4.2. *Probability density distributions of second-order moments*

The p.d.f. distributions of Reynolds shear stress uv and turbulent scalar flux $v\theta$ are shown in figures 5(a) and 5(b), respectively. The solid line shows the theoretical p.d.f. $P_{II}(x)$ for a second-order moment derived from (12). The p.d.f. of uv has been studied by Lu & Willmarth (1973), Antonia & Atkinson (1973) and Nakagawa & Nezu (1977), but a systematic investigation of the p.d.f. of $v\theta$ has not been performed so far.

The theoretical p.d.f. $P_{II}(x)$ can be obtained by differentiating a cumulative probability distribution function $F_{II}(x)$ with respect to x. In the case of $x = \hat{v}\hat{\theta}$, a definition of $F_{II}(x)$ is

$$F_{II}(x) = \text{Prob}\,\{\hat{v}\hat{\theta} < x\}. \tag{20}$$

The corresponding representation in the (v, θ)-plane yields

$$F_{\mathrm{II}}(x) = \int_{-\infty}^{0} \left[\int_{x/\hat{v}}^{\infty} \left\{ \int_{-\infty}^{\infty} P(\hat{u}, \hat{v}, \hat{\theta}) \, \mathrm{d}\hat{u} \right\} \mathrm{d}\hat{\theta} \right] \mathrm{d}\hat{v}$$

$$+ \int_{0}^{\infty} \left[\int_{-\infty}^{x/\hat{v}} \left\{ \int_{-\infty}^{\infty} P(\hat{u}, \hat{v}, \hat{\theta}) \, \mathrm{d}\hat{u} \right\} \mathrm{d}\hat{\theta} \right] \mathrm{d}\hat{v}. \quad (21)$$

Differentiation of (21) with respect to x leads to

$$P_{\mathrm{II}}(\hat{v}\hat{\theta}) = \frac{\mathrm{d}F_{\mathrm{II}}(x)}{\mathrm{d}x}$$

$$= \int_{0}^{\infty} \left[\int_{-\infty}^{\infty} \left\{ P\left(\hat{u}, -\hat{v}, \frac{-x}{\hat{v}} \right) + P\left(\hat{u}, \hat{v}, \frac{x}{\hat{v}} \right) \right\} \mathrm{d}\hat{u} \right] \frac{\mathrm{d}\hat{v}}{\hat{v}}$$

$$= \frac{1}{\pi} \sum_{\substack{q+r=\mathrm{even}}}^{K \leqslant 4} C_{0qr} \int_{0}^{\infty} H_q(\hat{v}) H_r\left(\frac{x}{\hat{v}} \right) \exp\left[-\frac{1}{2} \left\{ \hat{v}^2 + \left(\frac{x}{\hat{v}} \right)^2 \right\} \right] \frac{\mathrm{d}\hat{v}}{\hat{v}}. \quad (22)$$

Similarly, the p.d.f. for $\hat{u}\hat{v}$ is derived as

$$P_{\mathrm{II}}(\hat{u}\hat{v}) = \frac{1}{\pi} \sum_{\substack{p+q=\mathrm{even}}}^{K \leqslant 4} C_{pq0} \int_{0}^{\infty} H_p(\hat{u}) H_q\left(\frac{x}{\hat{u}} \right) \exp\left[-\frac{1}{2} \left\{ \hat{u}^2 + \left(\frac{x}{\hat{u}} \right)^2 \right\} \right] \frac{\mathrm{d}\hat{u}}{\hat{u}}. \quad (23)$$

As shown in figure 5, though oppositely skewed, the distributions of $P_{\mathrm{II}}(\hat{u}\hat{v})$ and $P_{\mathrm{II}}(\hat{v}\hat{\theta})$ are seen to be similar in every respect. The shapes of the p.d.f.s change little with radial location, from within the wall region out to the core region of the flow, which corresponds to constancy in correlation coefficients ($R_{uv} \approx -0.5$ and $R_{v\theta} \approx 0.5$) over these regions (Hishida *et al.* 1986). The long tails of the p.d.f.s substantiate the highly intermittent nature of momentum and scalar transfer. At the pipe centreline, R_{uv} and $R_{v\theta}$ are zero, and both $P_{\mathrm{II}}(\hat{u}\hat{v})$ and $P_{\mathrm{II}}(\hat{v}\hat{\theta})$ distributions become symmetrical. It is evident from figure 5(a, b) that the theoretical predictions from (22) and (23) follow the experimental trend quite closely.

4.3. *Turbulent diffusion of turbulence energy components, scalar variance, Reynolds shear stress and turbulent scalar fluxes*

4.3.1. *Comparison of measurements of turbulent diffusion with predictions by existing models for triple products*

The distributions of turbulent diffusion, i.e. third-order moments, of turbulence energy components u^2 and v^2, scalar variance θ^2, Reynolds shear stress uv, and turbulent scalar fluxes $u\theta$ and $v\theta$ are presented in figures 6(a, b). The values predicted from the existing models for triple products $\overline{uuv}$ and $\overline{vv\theta}$, i.e. diffusion of uv and $v\theta$, are included in figure 6 to evaluate the performance of the models. A prime denotes the normalization of velocity and scalar (temperature) by the friction velocity and friction temperature, respectively. The representative existing models are as follows:

(i) Models for turbulent diffusion of Reynolds stress $\overline{u_i u_j u_k}$:

(a) Daly & Harlow(1970)

$$\overline{u_i u_j u_k} = -C_{R1} \frac{k}{\epsilon} \overline{u_k u_l} \frac{\partial \overline{u_i u_j}}{\partial x_l}; \quad (24)$$

(b) Hanjalić & Launder (1972)

$$\overline{u_i u_j u_k} = -C_{R2} \frac{k}{\epsilon} \left[\overline{u_l u_j} \frac{\partial \overline{u_i u_k}}{\partial x_l} + \overline{u_l u_i} \frac{\partial \overline{u_j u_k}}{\partial x_l} + \overline{u_l u_k} \frac{\partial \overline{u_i u_j}}{\partial x_l} \right]; \quad (25)$$
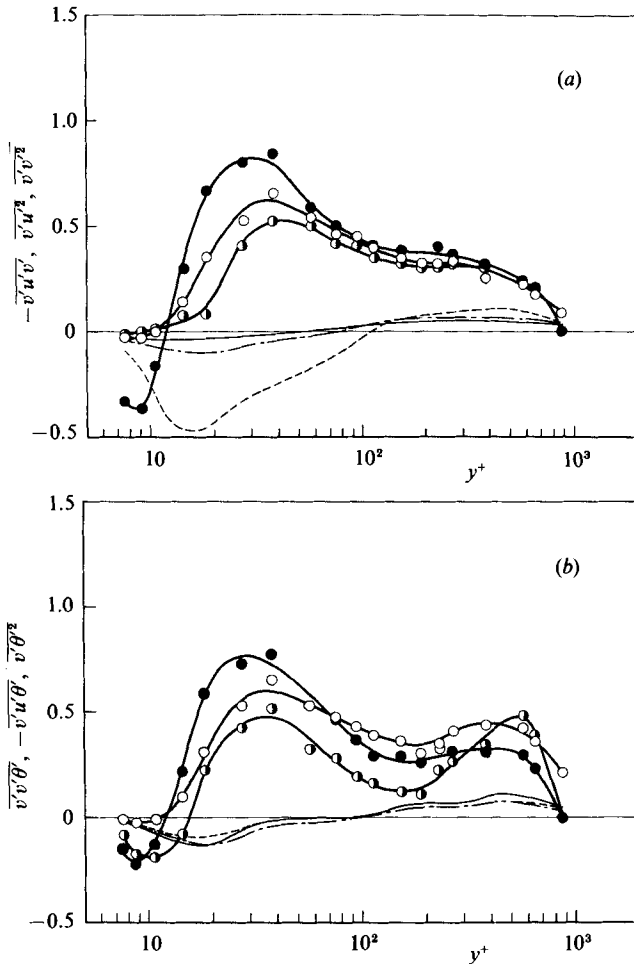
Figure 6. Distributions of turbulent diffusion (third-order moments). (*a*) Velocity field. Experiments: —○—, $-\overline{vuv}$; —●—, $\overline{vu^2}$; —◑—, $\overline{vv^2}$. Predictions for $-\overline{vuv}$: ——, Daly & Harlow (1970); —·—, Hanjalić & Launder (1972); ---, Cormack *et al.* (1978). (*b*) Scalar field. Experiments: —○—, $\overline{vv\theta}$; —●—, $-\overline{vu\theta}$; —◑—, $\overline{v\theta^2}$. Predictions for $\overline{vv\theta}$: ——, Owen (1973); —·—, Deardorff (1973); ---, Wyngaard & Coté (1974).

(*c*) Cormack, Leal & Seinfeld (1978)

$$\overline{u_i u_j u_k} = \frac{4k^2}{\epsilon}\left\{2\alpha_1(\delta_{ij}\delta_{kl}+\delta_{ik}\delta_{jl}+\delta_{kj}\delta_{il})\frac{\partial k}{\partial x_l}+\alpha_2\left(\frac{\partial a_{ik}}{\partial x_j}+\frac{\partial a_{ij}}{\partial x_k}+\frac{\partial a_{kj}}{\partial x_i}\right)\right\} \\ +\frac{2k}{\epsilon}\left\{2\alpha_3(\delta_{ik}a_{jl}+\delta_{ij}a_{kl}+\delta_{jk}a_{il})\frac{\partial k}{\partial x_l}\right. \\ \left.+\alpha_4\left(a_{ik}\frac{\partial a_{jl}}{\partial x_l}+a_{ij}\frac{\partial a_{kl}}{\partial x_l}+a_{kj}\frac{\partial a_{il}}{\partial x_l}\right)\right\}, \; a_{ij}=\overline{u_i u_j}-2\delta_{ij}k/3. \quad (26)$$

(ii) Models for turbulent diffusion of scalar flux $\overline{u_i u_j \theta}$:
(*a*) Deardorff (1973)

$$\overline{u_i u_j \theta} = -\frac{k}{\epsilon}\left[c_1\overline{u_j u_l}\frac{\partial\overline{u_i\theta}}{\partial x_l}+c_2\overline{u_i u_l}\frac{\partial\overline{u_j\theta}}{\partial x_l}+c_3\overline{u_l\theta}\frac{\partial\overline{u_i u_j}}{\partial x_l}\right], \quad (27)$$

Model for triple product	Constant	Value (present work)
Daly & Harlow (1970)	C_{R1}	0.21
Hanjalić & Launder (1972)	C_{R2}	0.11
Cormack et al. (1978)	α_1	-8.14×10^{-3}
(for all flows)	α_2	-1.72×10^{-2}
	α_3	-4.80×10^{-2}
	α_4	-1.02×10^{-1}
Deardorff (1973)	c_{s1}	0.11
Owen (1973)	c_{s2}	0.11
Wyngaard & Coté (1974)	c_{s3}	0.13
Wyngaard (1975)	c_{s3}	0.13

TABLE 1. Model constants used in the existing models for triple products
of velocity and scalar

with $c_1 = c_2 = c_3 = c_{s1}$;
    (b) Owen (1973)
letting $c_3 = 0$, $c_1 = c_2 = c_{s2}$ in (27);
    (c) Wyngaard & Coté (1974)
letting $c_2 = c_3 = 0$, $c_1 = c_{s3}$ in (27).
    (iii) Models for turbulent diffusion of scalar variance $\overline{u_j \theta^2}$:
    (a) Deardorff (1973)
letting $u_i = \theta$ in (ii) (a);
    (b) Wyngaard (1975)
letting $u_i = \theta$ in (ii) (c),

where k and ϵ are the turbulence kinetic energy ($= \frac{1}{2}\overline{u_i u_i}$) and dissipation rate of turbulence energy, respectively. All are definitely gradient-type diffusion models. The model constants used in the present study are summarized in table 1.

As shown in figure 6, turbulent diffusions pertaining to the velocity field are similarly distributed with maxima at approximately $y^+ \approx 30$. The same applies to turbulent diffusions for the scalar field, in which the second peaks are seen to exist in the outer region. Comparing the calculated values of $-\overline{uuv}$ and $\overline{vv\theta}$ from the existing models with the experimental results, we find that all models fail to predict the measurements quantitatively for $y^+ > 100$ and even qualitatively for $y^+ < 100$, where the predictions have the opposite trend to the measurements. Accordingly, there is a risk that serious errors may be introduced into the results of predictions if these models are incorporated in the Reynolds-stress and/or scalar-flux equation models.

4.3.2. Probability density distributions of third-order moments

To construct appropriate models, we need to investigate the statistical characteristics of third-order moments in detail and give a theoretical explanation for them. Figure 7 shows measurements of p.d.f. distributions of third-order moments. Every p.d.f. is nearly symmetrical about zero and has very long tails for positive and negative values of the abscissa, although not distributed in the Gaussian manner. Also, all of these distributions are too similar to be readily distinguished from others. This means that turbulent diffusion is a very intermittent phenomenon and that the magnitude and direction of time-averaged diffusion are determined by a delicate imbalance (i.e. asymmetry) of the p.d.f. distribution.
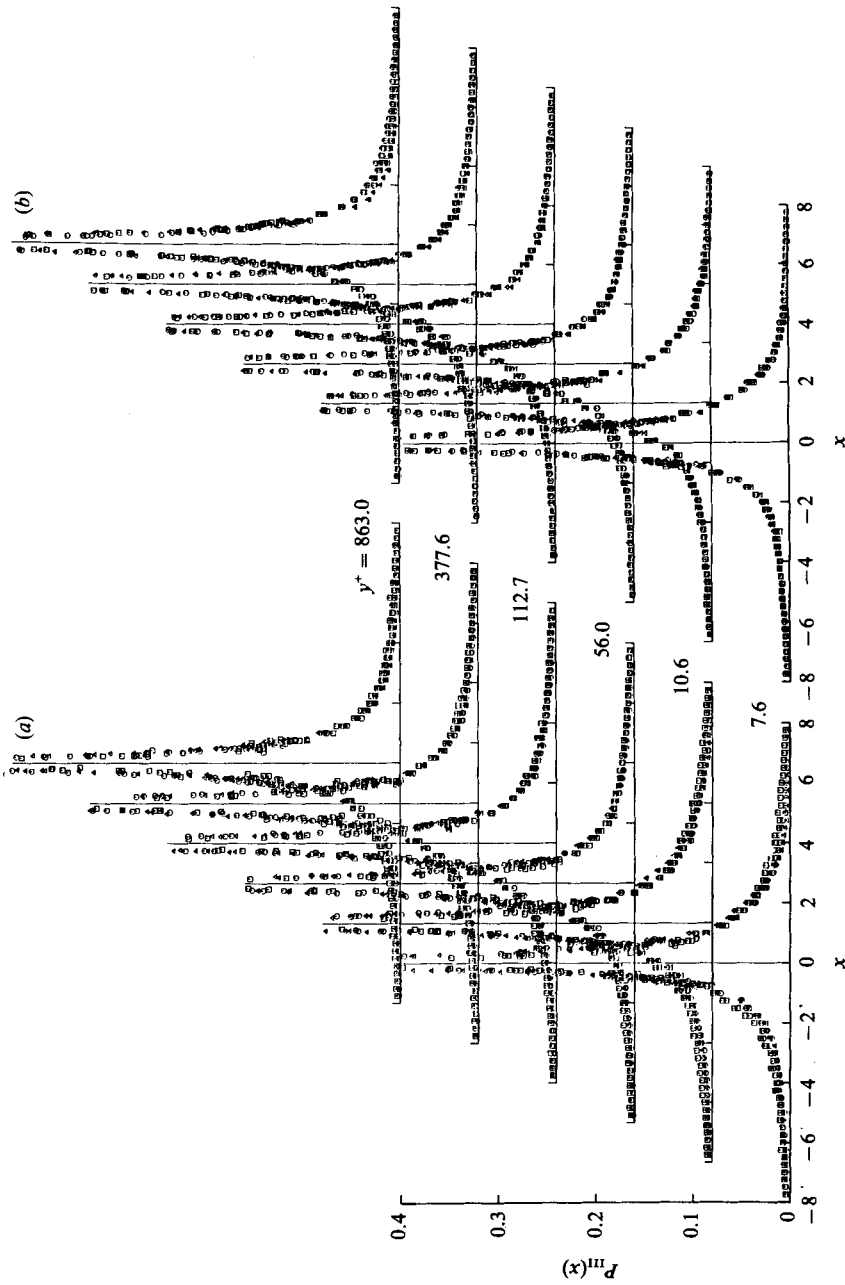
FIGURE 7. Probability density distributions of third-order moments. (a) Velocity field: $\odot$, $-\hat{v}\hat{u}\hat{v}$; $\triangle$, $\hat{v}\hat{u}^2$; $\square$, $\hat{v}\hat{v}^2$. (b) Scalar field: $\odot$, $\hat{v}\hat{v}\hat{\theta}$; $\triangle$, $-\hat{v}\hat{u}\hat{\theta}$; $\square$, $\hat{v}\hat{\theta}^2$.
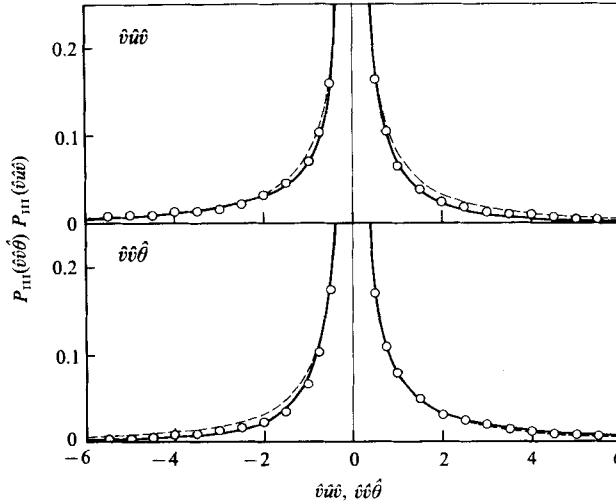
FIGURE 8. Comparison of predictions with experimental results for probability density of third-order moments ($y^+ = 37.1$). $\bigcirc$, experiments; ———, equation (28) for $P_{\mathrm{III}}(\hat{v}\hat{u}\hat{v})$ and equation (29) for $P_{\mathrm{III}}(\hat{v}\hat{v}\hat{\theta})$; — — —, Gaussian.

To illustrate this situation, we derive the theoretical p.d.f. distributions for third-order moments $P_{\mathrm{III}}(\hat{v}\hat{u}\hat{v})$, $P_{\mathrm{III}}(\hat{v}\hat{v}\hat{\theta})$ and $P_{\mathrm{III}}(\hat{v}\hat{u}\hat{\theta})$ from a non-Gaussian joint p.d.f. (12). Following the same procedure as for the second-order moments (cf. (22) and (23)), $P_{\mathrm{III}}(x)$ for $x = \hat{v}\hat{u}\hat{v}$, $\hat{v}\hat{v}\hat{\theta}$ and $\hat{v}\hat{u}\hat{\theta}$ are

$$
P_{\mathrm{III}}(\hat{v}\hat{u}\hat{v}) = \int_0^\infty \int_{-\infty}^\infty \left\{ P\left(\frac{x}{\hat{v}^2}, \hat{v}, \hat{\theta}\right) + P\left(\frac{x}{\hat{v}^2}, -\hat{v}, \hat{\theta}\right) \right\} \frac{\mathrm{d}\hat{\theta}\,\mathrm{d}\hat{v}}{\hat{v}^2}
$$

$$
= \frac{1}{\pi} \sum_{q=\mathrm{even}}^{K \leqslant 4} C_{pq0} \int_0^\infty H_p\left(\frac{x}{\hat{v}^2}\right) H_q(\hat{v}) \exp\left[-\frac{1}{2}\left\{\left(\frac{x}{\hat{v}^2}\right)^2 + \hat{v}^2\right\}\right] \frac{\mathrm{d}\hat{v}}{\hat{v}^2}, \qquad (28)
$$

$$
P_{\mathrm{III}}(\hat{v}\hat{v}\hat{\theta}) = \int_0^\infty \int_{-\infty}^\infty \left\{ P\left(\hat{u}, \hat{v}, \frac{x}{\hat{v}^2}\right) + P\left(\hat{u}, -\hat{v}, \frac{x}{\hat{v}^2}\right) \right\} \frac{\mathrm{d}\hat{u}\,\mathrm{d}\hat{v}}{\hat{v}^2}
$$

$$
= \frac{1}{\pi} \sum_{q=\mathrm{even}}^{K \leqslant 4} C_{0qr} \int_0^\infty H_q(\hat{v}) H_r\left(\frac{x}{\hat{v}^2}\right) \exp\left[-\frac{1}{2}\left\{\hat{v}^2 + \left(\frac{x}{\hat{v}^2}\right)^2\right\}\right] \frac{\mathrm{d}\hat{v}}{\hat{v}^2}, \qquad (29)
$$

$$
P_{\mathrm{III}}(\hat{v}\hat{u}\hat{\theta}) = \iint_0^\infty \left\{ P\left(\hat{u}, \hat{v}, \frac{x}{\hat{u}\hat{v}}\right) + P\left(-\hat{u}, \hat{v}, \frac{-x}{\hat{u}\hat{v}}\right) \right.
$$

$$
\left. + P\left(-\hat{u}, -\hat{v}, \frac{x}{\hat{u}\hat{v}}\right) + P\left(\hat{u}, -\hat{v}, \frac{-x}{\hat{u}\hat{v}}\right) \right\} \frac{\mathrm{d}\hat{u}\,\mathrm{d}\hat{v}}{\hat{u}\hat{v}}. \qquad (30)
$$

The p.d.f. based on an assumption of Gaussian behaviour, $P_{\mathrm{GIII}}(x)$, is similarly obtained, using (8) instead of (12).

The measured p.d.f. distributions of $\hat{v}\hat{u}\hat{v}$ and $\hat{v}\hat{v}\hat{\theta}$ are presented in figure 8, compared with the theoretical predictions from (28) and (29) and those based on a Gaussian joint p.d.f. Evidently, the asymmetry in p.d.f. distributions is fractional, but it is this asymmetry that determines the net value of turbulent diffusion. If a theory is developed on the basis of an assumption of Gaussian behaviour, the p.d.f.

distributions of third-order moments become symmetrical about zero. Consequently, time-averaged values of third-order moments (i.e. expectations of instantaneous third-order moments) are consistently zero, and the important characteristics of turbulent diffusion are not described fully. However, as seen from figure 8, the present theoretical models (28) and (29) can precisely predict the asymmetry in p.d.f. distributions, thus yielding the correct values of third-order moments.

5. Fine structure of the coherent turbulent transport process

5.1. *Classification of fluid motions*

To make clear the relation between the coherent structures and turbulent momentum and scalar transfer quantitatively, it is essential to properly extract well-ordered motions from superficially random time-series data of hot-wire measurement. Several kinds of detection algorithms have been proposed; each algorithm possesses its own special features so as to catch various aspects of the coherent structures. Recently, Bogard & Tiederman (1986) evaluated the capability of several representative detection algorithms using simultaneous measurements from a hot-wire and flow-visualization techniques in a wall-bounded flow. As a result, they concluded that a uv-quadrant method had the greatest reliability with a high probability of detecting the organized motions and a low probability of false detections.

In another paper (Nagano & Tagawa 1988), we developed an objective detection algorithm on the basis of a 'trajectory', i.e. a quadrant sequence of fluid motions classified in the (u, v)-plane. And it was demonstrated that typical vortex structures of wall turbulence, which had been identified by the flow-visualization techniques, could be reproduced precisely using this detection algorithm. For that reason, in the present study, we also use the uv-quadrant analysis (figure 9). According to this method, ejection- and sweep-type motions, which are the basic elements of coherent structures in wall turbulence, are classified into the second $(i = 2)$ and fourth quadrants $(i = 4)$, respectively. It should be mentioned here that ejections in the strict sense correspond to the second-quadrant motions with larger amplitudes (Bogard & Tiederman 1986). However, for simplicity, we refer to all quadrant-2 motions as ejections and all quadrant-4 motions as sweeps in this study.

5.2. *Conditional probability density distributions of velocity and scalar fluctuations*

Using the generalized three-dimensional joint p.d.f. developed in §3, we can obtain the following one-dimensional conditional p.d.f. $P_i(\chi)$ in terms of the flow-classification given in figure 9:

$$\left.\begin{aligned}
P_i(\hat{u}) &= \int_0^\infty \left\{ \int_{-\infty}^\infty P(\hat{u}, \sigma_{v,i}\hat{v}, \hat{\theta})\,\mathrm{d}\hat{\theta} \right\} \mathrm{d}\hat{v}, \\
P_i(\hat{v}) &= \int_0^\infty \left\{ \int_{-\infty}^\infty P(\sigma_{u,i}\hat{u}, \hat{v}, \hat{\theta})\,\mathrm{d}\hat{\theta} \right\} \mathrm{d}\hat{u}, \\
P_i(\hat{\theta}) &= \iint_0^\infty P(\sigma_{u,i}\hat{u}, \sigma_{v,i}\hat{v}, \hat{\theta})\,\mathrm{d}\hat{u}\,\mathrm{d}\hat{v},
\end{aligned}\right\} \tag{31}$$

where
$$\sigma_{u,i} = (1, -1, -1, 1), \quad \sigma_{v,i} = (1, 1, -1, -1). \tag{32}$$

Here, the suffix i denotes each quadrant in the (u, v)-plane, and $\sigma_{u,i}$ and $\sigma_{v,i}$ are sign
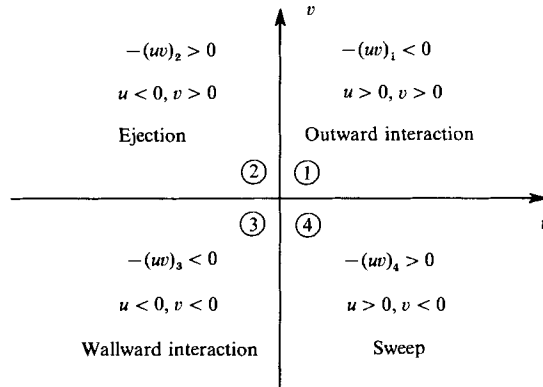
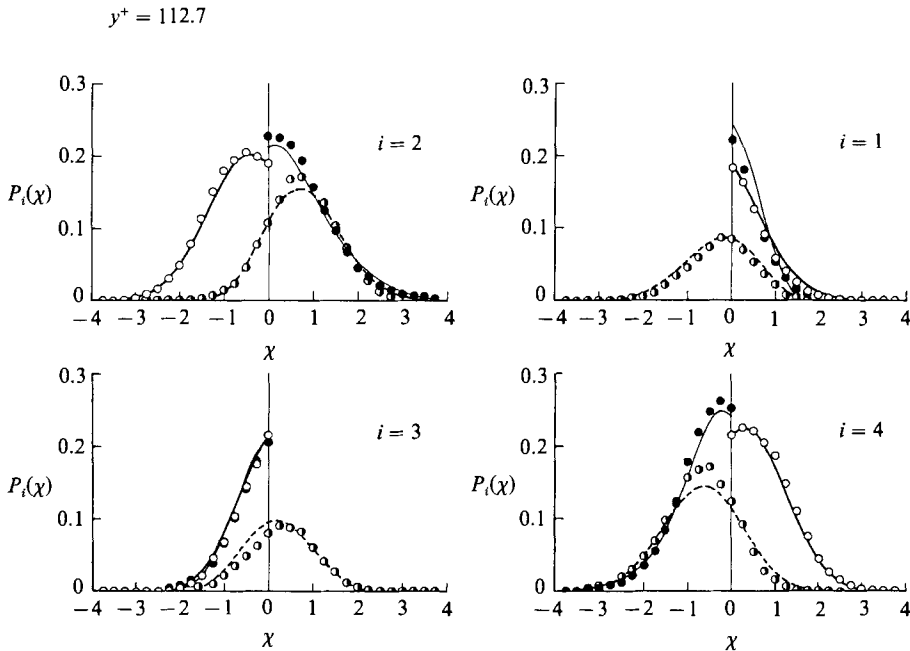FIGURE 9. Classification of fluid motions in the (u, v)-plane.

$y^+ = 112.7$

FIGURE 10. Conditional probability density distributions of velocity and scalar fluctuations. Experiments: $\bigcirc$, $P_i(\hat{u})$; $\bullet$, $P_i(\hat{v})$; $\circleddash$, $P_i(\hat{\theta})$. Predictions from equation (31): ———, $P_i(\hat{u})$; ———, $P_i(\hat{v})$; — — —, $P_i(\hat{\theta})$.

functions which represent the signs of u and v of the ith quadrant. For example, in the case $i = 2$, we have $(\sigma_{u,i}, \sigma_{v,i}) = (-1, 1)$.

The experimental results for $P_i(\chi)$ are shown in figure 10, compared with the values calculated from (31). The most probable value of the conditional p.d.f. of scalar fluctuations exists in the region $\theta > 0$ at an ejection phase $(i = 2)$ and in the region $\theta < 0$ at a sweep phase $(i = 4)$. This result provides statistical support for the evidence that low-momentum and high-enthalpy fluid moves away from the wall during the ejection phase and, inversely, high-momentum and low-enthalpy fluid moves toward the wall during the sweep phase. On the other hand, the conditional p.d.f.s $P_i(\hat{\theta})$ related to both interaction phases $(i = 1, 3)$ are almost symmetrical; that is, the scalar fluctuations do not correlate with the interactive fluid motions.

Predictions from (31) are seen to be in excellent agreement with the experimental values. Thus, we can apply the joint p.d.f. $P(\hat{u}, \hat{v}, \hat{\theta})$ to the analysis of the coherent turbulent structures and the relevant transport processes of momentum and scalar.

5.3. *Contributions of organized fluid motions to second-order moments*

5.3.1. *Contributions of different motions to turbulent momentum and scalar transfer*

Figures 11 and 12 respectively show the results of the fractional contributions to the time-averaged values of Reynolds shear stress $\overline{uv}$ and turbulent scalar flux $\overline{v\theta}$ from each fluid motion classified in the (u, v)-plane. The contributions from ejections become largest in the region $y^+ > 10$, while sweeps predominate in the near-wall region $(y^+ < 10)$. These features are equally seen in contributions to both $\overline{uv}$ and $\overline{v\theta}$. Lines in figures 11 and 12 represent the theoretical predictions from the following equation (33), which is obtained by calculating the moment $\overline{u^l v^m \theta^n}$ separately in each quadrant of the (u, v)-plane with (12):

$$(\overline{\hat{u}^l \hat{v}^m \hat{\theta}^n})_{i, H} = \sigma_{u, i}^l \sigma_{v, i}^m \int_0^\infty \left[\int_{H/\hat{u}}^\infty \left\{ \int_{-\infty}^\infty \hat{u}^l \hat{v}^m \hat{\theta}^n P(\sigma_{u, i} \hat{u}, \sigma_{v, i} \hat{v}, \hat{\theta}) \, d\hat{\theta} \right\} d\hat{v} \right] d\hat{u}$$

$$= \frac{2}{(2\pi)^{\frac{3}{2}}} \sum_{\substack{p, q, r=0 \\ n+r=\text{even}}}^{K \leqslant 4} \sigma_{u, i}^{l+p} \sigma_{v, i}^{m+q} C_{pqr} \left[\int_0^\infty b_{l, p}(\hat{u}) \left\{ \int_{H/\hat{u}}^\infty b_{m, q}(\hat{v}) \, d\hat{v} \right\} d\hat{u} \right] B_{n, r},$$

(33)

where $\qquad b_{j, k}(\chi) = \chi^j H_k(\chi) \exp\left(-\tfrac{1}{2}\chi^2\right), \quad B_{j, k} = \int_0^\infty b_{j, k}(\chi) \, d\chi,$

and the parameter H is a threshold so as to pick out phenomena only for $|\hat{u}\hat{v}| > H$. Putting $H = 0$, $l = m = 1$ and $n = 0$ for $\overline{(uv)}_i$, and $H = 0$, $m = n = 1$ and $l = 0$ for $\overline{(v\theta)}_i$ in (33), we obtain the theoretical values shown in figures 11 and 12, respectively. As seen in these figures, the theoretical predictions correspond with the experimental trends satisfactorily. Thus, essential aspects of the coherent structures, such as negligible contributions from both interactions and a reversal of contributions in ejections and sweeps at about $y^+ = 10$, are well reproduced.

The scales of fluid motions which contribute mainly to the turbulent scalar transport are presented in figure 13, being evaluated using a threshold level H. From this figure, one can recognize that the scalar transport processes are dominated by large-amplitude ejection- and sweep-type coherent motions, and the contributions of both interactions are negligible for $H > 2$. Nakagawa & Nezu (1977) used a two-dimensional p.d.f. for analysing the structures of Reynolds shear stress $\overline{uv}$ theoretically. However, in order to clarify the structures of turbulent scalar fluxes in terms of typical turbulent motions classified in the (u, v)-plane, we need a three-dimensional p.d.f. Hence, their approach is not applicable for this purpose. The lines in figure 13 show the predictions from (33) for various threshold levels. Clearly, (33) is very useful for analysing the turbulent scalar transfer in conjunction with the scales of fluid motions.

5.3.2. *Conditional probability density distribution of scalar flux $v\theta$*

As stated previously, turbulent scalar flux $v\theta$ is determined by large-amplitude organized motions (ejections and sweeps). To gain a deeper insight into this distinct feature, we have investigated the conditional p.d.f. of $v\theta$ (figure 14a) and the conditional weighted distribution defined as $\hat{v}\hat{\theta}[P_{\text{II}, i}(\hat{v}\hat{\theta})]$ (figure 14b) in the buffer region $(y^+ = 10.6)$ where the organized motions are prominent. The distribution of
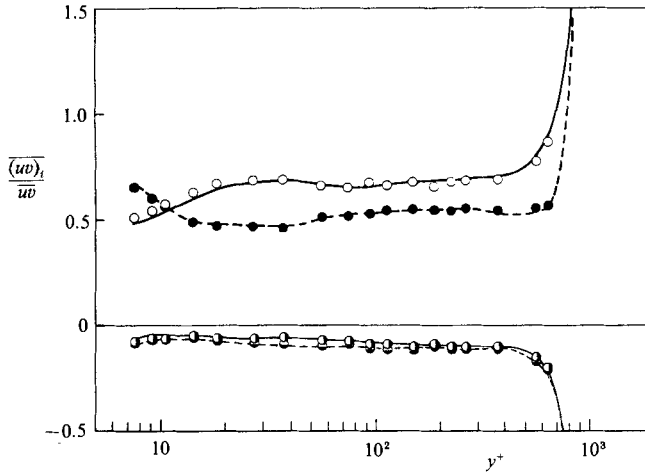
FIGURE 11. Fractional contributions of different motions to the time-averaged value of Reynolds shear stress $-\overline{uv}$. Experiments: $\CIRCLE$, $i = 1$; $\bigcirc$, $i = 2$; $\ominus$, $i = 3$; $\bullet$, $i = 4$. Predictions from equation (33): ——, $i = 1$; ——, $i = 2$; –––, $i = 3$; ———, $i = 4$.
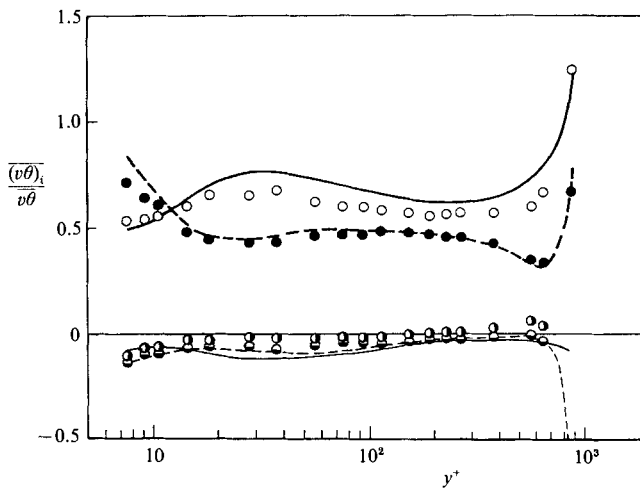

FIGURE 12. Fractional contributions of different motions to the time-averaged value of turbulent scalar flux $\overline{v\theta}$. Notation as in figure 11.

$\hat{v\theta}[P_{\mathrm{II},i}(\hat{v\theta})]$ represents a statistical contribution to the total scalar flux $\overline{v\theta}$ from various amplitudes of $\hat{v\theta}$ fluctuations. As is obvious from figure 14(a), ejections ($i = 2$) and sweeps ($i = 4$) are the principal contributors to the time-averaged scalar flux $\overline{v\theta}$, since the conditional p.d.f.s in the ejection and sweep phase are skewed largely to the positive side of $v\theta$. At this y-location, the fractional contributions of ejections and sweeps are nearly equal (see figure 12). However, figure 14(b) indicates that the detailed structure of ejections and sweeps differs somewhat. Larger-amplitude fluctuations of turbulent scalar flux ($\hat{v\theta} > 2.5$) are mainly associated with the sweep-type coherent motions. Furthermore, figure 14(a, b) also proves that organized motions (ejections and sweeps) sometimes contribute negatively to the time-averaged value $\overline{v\theta}$. This means that a passive-scalar field does not necessarily
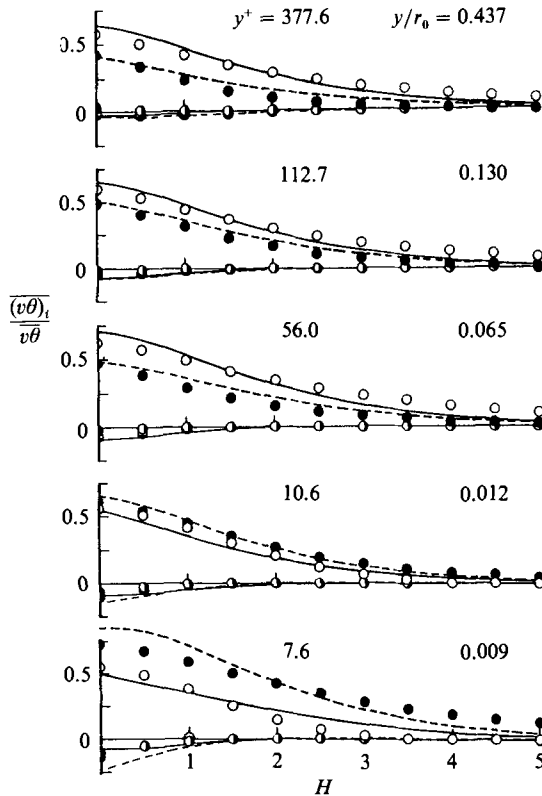
FIGURE 13. Fractional contributions of different motions to $\overline{v\theta}$ as a function of H. Notation as in figure 11.

follow a velocity field in a wall turbulent shear flow. In both interaction phases ($i = 1, 3$), the distributions of conditional p.d.f.s are seen to be much more symmetrical, and the correspondence between turbulent scalar transfer and fluid motions is very weak. Hence, the fractional contributions to $\overline{v\theta}$ from both interactions remain very low.

The lines in figure 14 (*a*) show theoretical values calculated from the following equation, (34), which is obtained by applying the same procedure as in the derivation of the p.d.f. for a second-order moment from the three-dimensional joint p.d.f.:

$$P_{\mathrm{II},i}(\hat{v}\hat{\theta}) = \iint_0^\infty P\left(\sigma_{u,i}\,\hat{u}, \sigma_{v,i}\,\hat{v}, \sigma_{v,i}\frac{x}{\hat{v}}\right)\left(\frac{\mathrm{d}\hat{v}}{\hat{v}}\right)\mathrm{d}\hat{u}$$

$$= \frac{1}{(2\pi)^{\frac{3}{2}}} \sum_{p,q,r=0}^{K\leqslant 4} \sigma_{u,i}^p\,\sigma_{v,i}^{q+r}\,C_{pqr}\,B_{0,p}$$

$$\times \int_0^\infty H_q(\hat{v})H_r\left(\frac{x}{\hat{v}}\right)\exp\left[-\frac{1}{2}\left\{\hat{v}^2+\left(\frac{x}{\hat{v}}\right)^2\right\}\right]\frac{\mathrm{d}\hat{v}}{\hat{v}}. \tag{34}$$

The appreciable discrepancy between the theories and measurements can be attributed to a small truncation effect in the series expansion for the joint p.d.f.
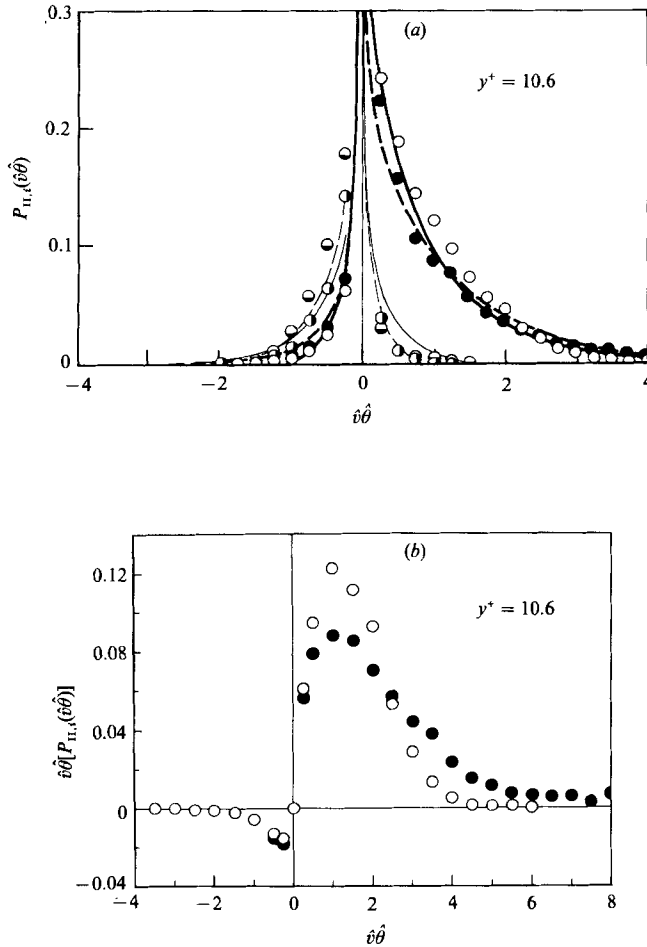
FIGURE 14. (a) Conditional probability density distribution of scalar flux $\hat{v}\hat{\theta}$. Experiments: $\mathbb{O}$, $i = 1$; $\bigcirc$, $i = 2$; $\ominus$, $i = 3$; $\bullet$, $i = 4$. Predictions from equation (34): ——, $i = 1$; ——, $i = 2$; – – –, $i = 3$; – – –, $i = 4$. (b) Experimental distributions of $\hat{v}\hat{\theta}[P_{\mathrm{II},i}(\hat{v}\hat{\theta})]$ representing a fractional contribution to the scalar flux $\overline{v\theta}$. $\bigcirc$, $i = 2$; $\bullet$, $i = 4$.

5.3.3. Weighted functions in the (u, v)-plane

The conditional analysis based on threshold H alone is not sufficient to ascertain the detailed correspondence between momentum/scalar transfer and fluid motions. Therefore, we define the following weighted function $W_x(\hat{u}, \hat{v})$ in the (u, v)-plane:

$$\left.\begin{aligned} W_x(\hat{u}, \hat{v}) &= \int_{-\infty}^{\infty} x P(\hat{u}, \hat{v}, \hat{\theta})\, \mathrm{d}\hat{\theta}, \\ x &= \hat{u}^l \hat{v}^m \hat{\theta}^n. \end{aligned}\right\} \tag{35}$$

This function provides a powerful tool to see how, and how much, each fluid motion in the quadrants of the (u, v)-plane produces the moment x. The integrated value of W_x in each quadrant becomes the fractional contribution $(x)_i$, and integration over the whole (u, v)-plane reduces to the conventional time-averaged value $\bar{x}$.

The experimental distributions of the weighted function for $x = \hat{\theta}^2$ are shown in figure 15. In the immediate neighbourhood of the wall ($y^+ = 7.6$), the distribution
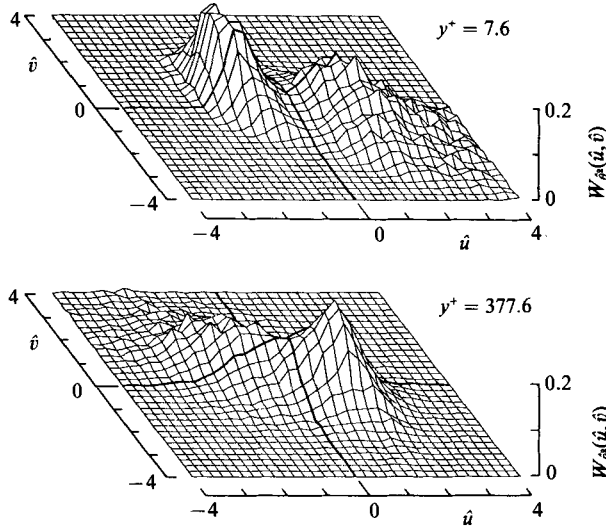
FIGURE 15. Experimental distributions of the weighted function for scalar variance $\overline{\theta^2}$.

extends far into the fourth quadrant (sweep phase), and peaks in the second quadrant (ejection phase) as if u-fluctuations were limited at $\hat{u} = -2$. In the core region of the flow ($y^+ = 377.6$), on the other hand, the distribution becomes wider, gently sloping in the second quadrant, and becoming narrower and steeper in the fourth quadrant. In another paper (Nagano & Tagawa 1988), it was shown that the contributions to scalar variance $(\overline{\theta^2})_i$ from sweeps were largest in the vicinity of the wall, and became almost equal to those from ejections in the core region. However, figure 15 demonstrates the existence of a definite difference in the internal structures of scalar variance $\overline{\theta^2}$, which cannot be identified from the conventional fractional contributions $(\overline{\theta^2})_i$. Hence, the mechanisms of the contribution from ejections and sweeps to the production of scalar variance in the near-wall region are totally different from those in the core region. Moreover, one can recognize that, even if the fractional contributions from ejections and sweeps are equal, there is a large difference in the scales of both motions governing the production of scalar fluctuations.

The experimental results for $W_{\hat{u}\hat{v}}$ and $W_{\hat{v}\hat{\theta}}$ in the near-wall region and for $W_{\hat{v}\hat{\theta}}$ in the core region are shown in figure 16(a–c), respectively. In the contour maps of figure 16, solid and broken lines represent positive and negative values, and intervals between two successive contour lines are 0.02. With figure 16(a, b), we can investigate the internal structures of the production processes of $\overline{uv}$ and $\overline{v\theta}$ near the wall. Integration of $W_{\hat{u}\hat{v}}$ and $W_{\hat{v}\hat{\theta}}$ within each quadrant results in the fractional contributions of different motions with $H = 0$ presented in figures 11 and 12, respectively. Also, integration of $W_{\hat{v}\hat{\theta}}$ over the region outside the hyperbolic boundary $\hat{v} = \pm H/\hat{u}$ results in the fractional contributions to $\overline{v\theta}$ from different motions as a function of H shown in figure 13. Thus, figure 16 contains a great deal of information.

As seen from these figures, the sweep-type motions with large-amplitude u-fluctuations dominate the production of $\overline{uv}$ and $\overline{v\theta}$ in the near-wall region. The distributions have characteristics similar to the scalar variance (figure 15; $y^+ = 7.6$). However, whereas both interactions ($i = 1, 3$) make a positive contribution to the
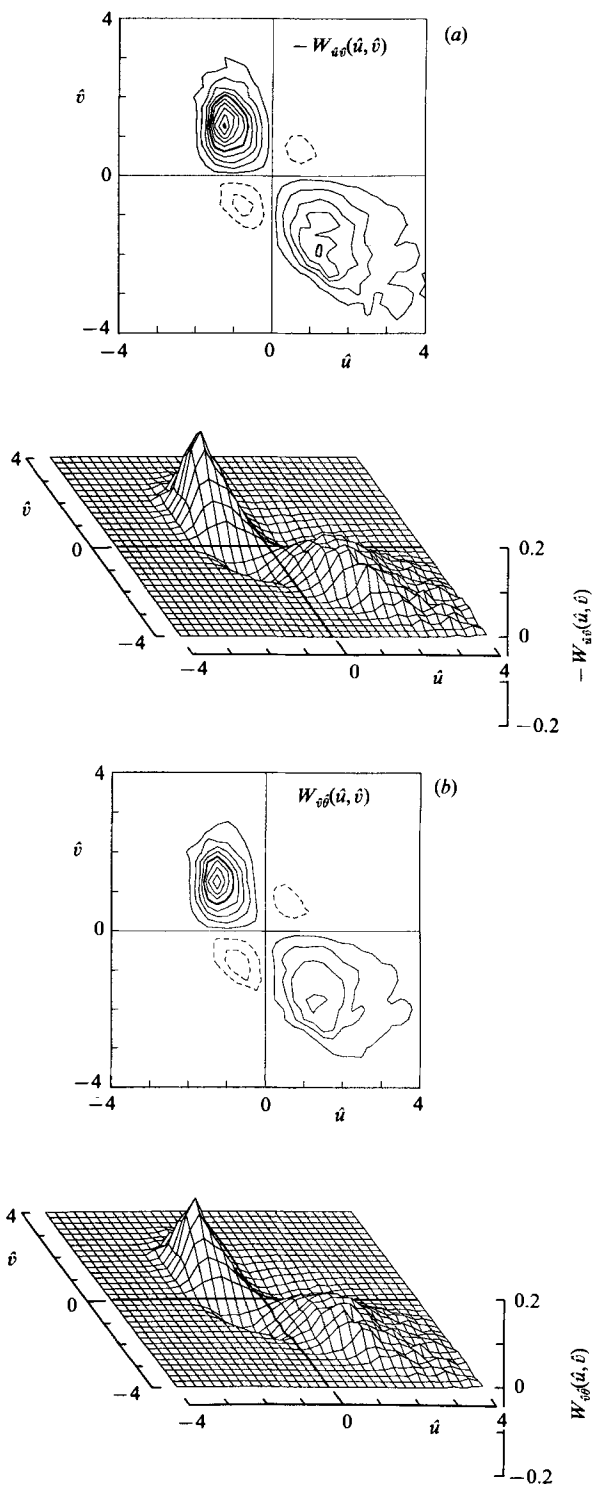
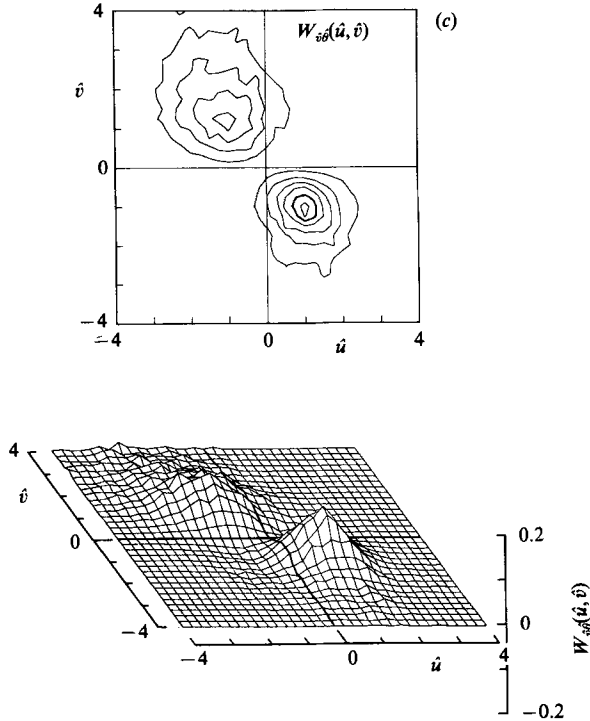FIGURE 16(a, b). For caption see facing page.

FIGURE 16. Experimental distributions of the weighted functions for turbulent momentum and scalar transfer. (a) $W_{\hat{u}\hat{v}}$ in the near-wall region ($y^+ = 7.6$); (b) $W_{\hat{v}\theta}$ in the near-wall region ($y^+ = 7.6$); (c) $W_{\hat{v}\theta}$ in the core region ($y^+ = 377.6$).

production of scalar variance $\overline{\theta^2}$, they contribute negatively to the Reynolds shear stress $-\overline{uv}$ and turbulent scalar flux $\overline{v\theta}$. Profiles shown in figure 16(a, b) are too similar to be readily distinguished from one another. This is an important result which shows that a close analogy exists between the internal structures of $\overline{uv}$ and $\overline{v\theta}$.

The distribution of $W_{\hat{v}\theta}$ in the core region (figure 16c) is different from that in the near-wall region (figure 16b) in the following respects: (i) the distributions in the second and fourth quadrants exhibit opposite trends; (ii) the negative regions seen in the first and third quadrants of figure 16(b) disappear in figure 16(c). The internal structures of $W_{\hat{v}\theta}$ change with the distance from the wall as in scalar variance, and the analogy between Reynolds shear stress and turbulent scalar flux breaks down with increasing distance from the wall. Note that Reynolds shear stress $-uv$ is consistently negative in the first and third quadrants.

5.4. *Contribution of organized motions to third-order moments*

In §4.3.2, we have shown that the p.d.f. distributions of third-order moments (i.e. turbulent diffusion of turbulence energy, scalar variance, turbulent scalar fluxes, etc.) have very long tails and the asymmetry in these p.d.f.s is fractional, but it is this asymmetry that determines the net value of turbulent diffusion. In this section, we elucidate their internal structures.

The contributions to $\overline{vu^2}$ and $\overline{v\theta^2}$ from different fluid motions with $H = 0$ are presented in figures 17(a) and 17(b), respectively. Obviously, the turbulent diffusion
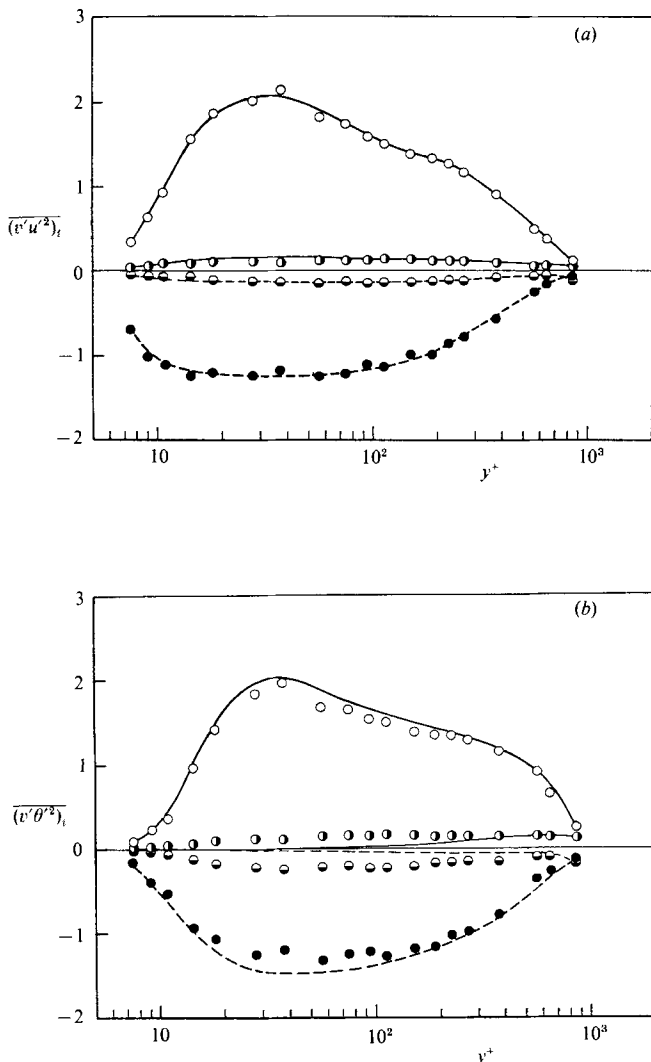
FIGURE 17. Contributions of organized motions to third-order moments $\overline{vu^2}$ and $\overline{v\theta^2}$. Notation as in figure 11. (a) $\overline{(vu^2)}_i$; (b) $\overline{(v\theta^2)}_i$.

of u^2 and θ^2 occurs mainly during the ejection and sweep phases ($i = 2, 4$), and hence the disparity in contributions between these two types of motions determines the magnitude and direction (i.e. plus and minus) of time-averaged diffusion. Neither interaction ($i = 1, 3$) influences the time-averaged values $\overline{vu^2}$ and $\overline{v\theta^2}$, since the fractional contributions from these motions are not only very small in absolute value but nearly symmetrical about zero (sum being zero). It is now established that the turbulent diffusion is determined by dynamic phenomena associated with organized motions of ejections and sweeps. This also explains why the third-order moments cannot be described adequately by a static model such as gradient-type diffusion of the second-order moment (see §4.3.1). The theoretical values in figure 17, calculated from (33), reproduce this dynamic behaviour very well. On the other hand, if a Gaussian distribution is supposed for the joint p.d.f. in (33), the contributions to the third-order moments from motions in the second and fourth quadrants of the (u, v)-
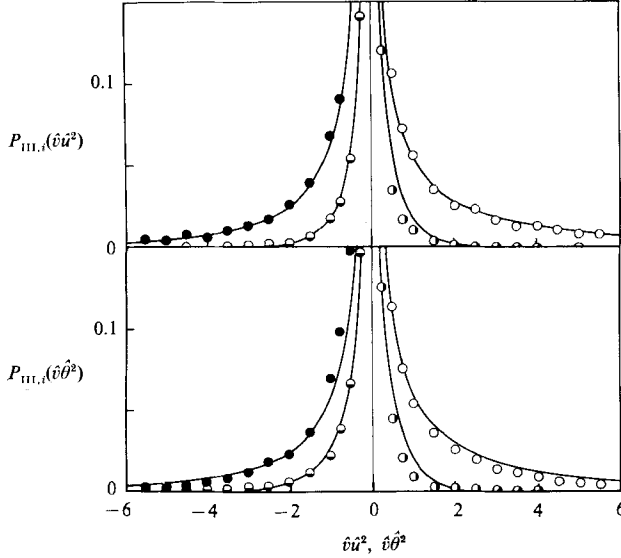
FIGURE 18. Conditional probability density distributions of the third-order moments $\hat{v}\hat{u}^2$ and $\hat{v}\hat{\theta}^2$ ($y^+ = 37.1$). Experiments: ◐, $i = 1$; ○, $i = 2$; ◕, $i = 3$; ●, $i = 4$. ———, predictions from equation (36) for $\hat{v}\hat{u}^2$ and equation (37) for $\hat{v}\hat{\theta}^2$.

plane are completely equal in magnitude, with an opposite sign. Hence, the foregoing important characteristics of third-order moments cannot be described fully.

To assess the feasibility of predicting the characteristics of the third-order moments theoretically in conjunction with the scales of fluid motions, we have examined the experimental distributions of the conditional p.d.f. of vu^2 and $v\theta^2$ at $y^+ = 37.1$ where the net values of the turbulent diffusion have their maxima (see figure 6). Figure 18 shows the measurements, compared with the present predictions. Solid lines in this figure represent the following theoretical distributions, which are obtained after differentiating the cumulative p.d.f.s for vu^2 and $v\theta^2$:

$$P_{\mathrm{III},i}(\hat{v}\hat{u}^2) = \int_0^\infty \left\{ \int_{-\infty}^\infty P\left(\sigma_{u,i}\hat{u}, \frac{x}{\hat{u}^2}, \hat{\theta}\right) \mathrm{d}\hat{\theta} \right\} \frac{\mathrm{d}\hat{u}}{\hat{u}^2}$$

$$= \frac{1}{2\pi} \sum_{p,q=0}^{p+q \leqslant 4} \sigma_{u,i}^p C_{pq0} \int_0^\infty H_p(\hat{u}) H_q\left(\frac{x}{\hat{u}^2}\right) \exp\left[-\frac{1}{2}\left\{\hat{u}^2 + \left(\frac{x}{\hat{u}^2}\right)^2\right\}\right] \frac{\mathrm{d}\hat{u}}{\hat{u}^2}, \quad (36)$$

where $x = \hat{v}\hat{u}^2$;

$$P_{\mathrm{III},i}(\hat{v}\hat{\theta}^2) = \int_0^\infty \left\{ \int_{-\infty}^\infty P\left(\sigma_{u,i}\hat{u}, \frac{x}{\hat{\theta}^2}, \hat{\theta}\right) \frac{\mathrm{d}\hat{\theta}}{\hat{\theta}^2} \right\} \mathrm{d}\hat{u}$$

$$= \frac{2}{(2\pi)^{\frac{3}{2}}} \sum_{\substack{p,q=0 \\ r=\mathrm{even}}}^{K \leqslant 4} \sigma_{u,i}^p C_{pqr} B_{0,p}$$

$$\times \int_0^\infty H_q\left(\frac{x}{\hat{\theta}^2}\right) H_r(\hat{\theta}) \exp\left[-\frac{1}{2}\left\{\left(\frac{x}{\hat{\theta}^2}\right)^2 + \hat{\theta}^2\right\}\right] \frac{\mathrm{d}\hat{\theta}}{\hat{\theta}^2} \quad (37)$$
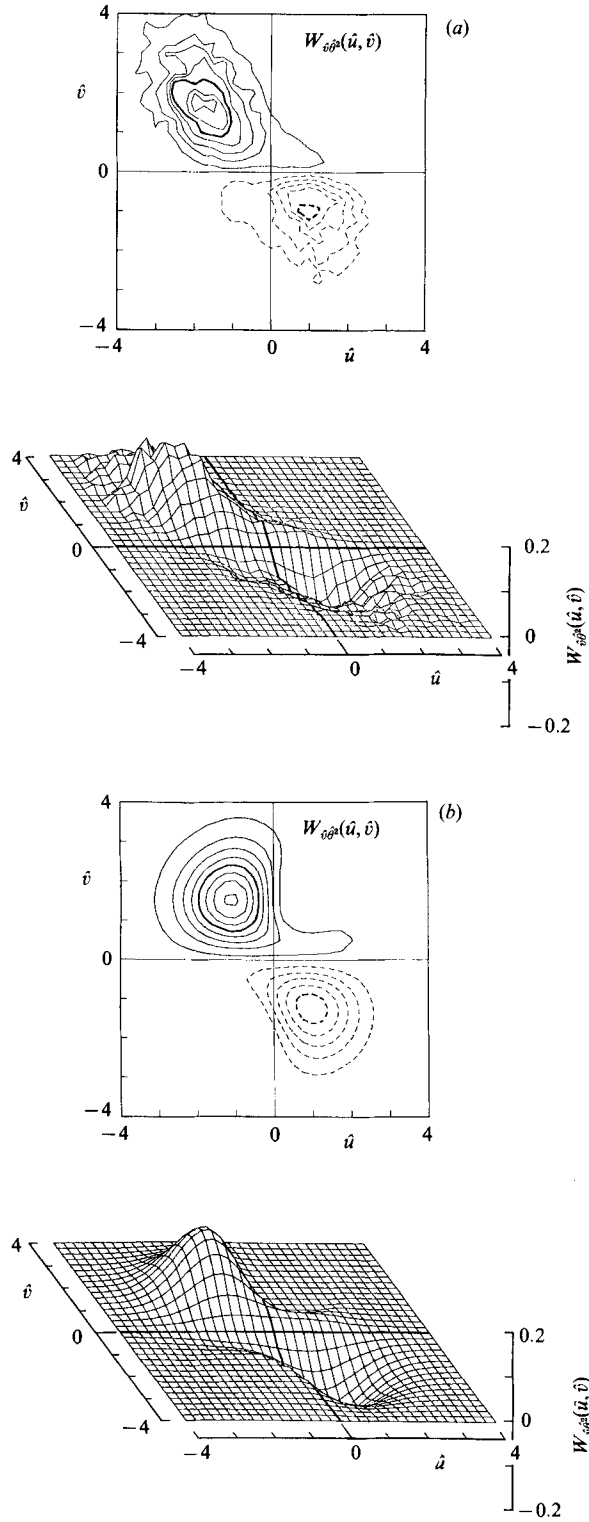
where $x = \hat{v}\hat{\theta}^2$.

FIGURE 19. Experimental and theoretical distributions of the weighted function for $\overline{v\theta^2}$ ($y^+ = 37.1$). (a) Experiment; (b) prediction.

It can be seen from the measured distributions that both conditional p.d.f.s of vu^2 and $v\theta^2$ at small $|x|$-values are a bit larger in the sweep phase than in the ejection phase, and vice versa at larger $|x|$-values. Since the fractional contributions $\overline{(vu^2)}_i$ and $\overline{(v\theta^2)}_i$ are obtained from the integration of (36) and (37) multiplied by x, the conditional p.d.f.s at larger $|x|$-values contribute mainly to these quantities. Accordingly, since large-amplitude fluctuations of vu^2 and $v\theta^2$ are generated mainly by ejections, the fractional contributions from ejections become larger than those from sweeps, as seen in figure 17. Such phenomena are well reproduced by the theoretical conditional p.d.f.s given by (36) and (37).

The experimental and theoretical distributions of the weighted function (35) for $v\theta^2$ are shown in figures 19(a) and 19(b), respectively. From the experimental result, one can see that the large-amplitude ejections contribute mainly to the production of $\overline{v\theta^2}$. Apparently, the theoretical results reproduce precisely the peak locations and the extent of the distributions in the second and fourth quadrants.

6. Conclusions

The statistical characteristics of momentum and scalar transfer in a wall turbulent shear flow have been investigated experimentally and theoretically. The results can be summarized as follows.

(i) A three-dimensional joint p.d.f. has been developed to describe the transfer processes of momentum and scalar in a two-dimensional turbulence field.

(ii) The p.d.f. distributions of u- and θ-fluctuations can be approximated with Gaussian ones in the log-law region, but in the other region they are skewed to the opposite sides. The probability distribution of v-fluctuations differs from a Gaussian distribution over a greater part of the flow field.

(iii) The skewness factor can be represented by the time fractions (i.e. intermittency factor) occupied by positive and negative events of a turbulence component.

(iv) The p.d.f. distributions of Reynolds shear stress uv and turbulent scalar flux $v\theta$ are similar, and change little over the entire cross-section except for the pipe-centreline region.

(v) The distributions of turbulent diffusion of $uv, v\theta, \theta^2$, etc. have been measured and compared with predictions from the existing models for triple products. All existing models are found to give quite unsatisfactory predictions for diffusion of uv and $v\theta$.

(vi) A net value of turbulent diffusion is determined by the fractional asymmetry of the p.d.f. distribution. This asymmetry cannot be reproduced by a Gaussian p.d.f. but can be represented by the p.d.f. developed in the present study.

(vii) The theoretical formulations for the conditional p.d.f. and the fractional contributions to various moments are derived using the three-dimensional joint p.d.f. These equations are applicable to the structural analysis of velocity and scalar fluctuations and their high-order moments.

(viii) Scalar fluctuations are influenced strongly by the organized motions of ejections and sweeps, but correlate little with interaction-type motions.

(ix) In the near-wall region $y^+ < 10$, the sweeps play a dominant role in the production processes of Reynolds shear stress $\overline{uv}$ and turbulent scalar flux $\overline{v\theta}$; the ejections predominate in the remaining region.

(x) In the near-wall region, there is a close analogy between the instantaneous structures of Reynolds shear stress uv and turbulent scalar flux $v\theta$.

(xi) The net values of turbulent diffusion in turbulence energy, scalar variance, turbulent scalar fluxes, etc. are determined by an imbalance between the contributions from ejections and sweeps. This can be well predicted by the present theory.

REFERENCES

ANTONIA, R. A. & ATKINSON, J. D. 1973 High-order moments of Reynolds shear stress fluctuations in a turbulent boundary layer. *J. Fluid Mech.* **58**, 581–593.

BOGARD, D. G. & TIEDERMAN, W. G. 1986 Burst detection with single-point velocity measurements. *J. Fluid Mech.* **162**, 389–413.

CORMACK, D. E., LEAL, L. G. & SEINFELD, J. H. 1978 An evaluation of mean Reynolds stress turbulence models: The triple velocity correlation. *Trans. ASME* I: *J. Fluids Engng* **100**, 47–54.

DALY, B. J. & HARLOW, F. H. 1970 Transport equations in turbulence. *Phys. Fluids* **13**, 2634–2649.

DEARDORFF, J. W. 1973 Three-dimensional numerical modeling of the planetary boundary layer. In *Proc. Workshop on Micrometeorology*, pp. 271–311. American Meteorological Society.

DURST, F., JOVANOVIC, J. & KANEVCE, LJ. 1987 Probability density distribution in turbulent wall boundary-layer flows. In *Turbulent Shear Flows* 5, pp. 197–220. Springer.

ELGHOBASHI, S. E. & LAUNDER, B. E. 1981 Modelling the dissipation rate of temperature variance in a thermal mixing layer. In *Proc. 3rd Intl Symp. on Turbulent Shear Flows*, pp. 15.13–15.17, University of California, Davis.

FRENKIEL, F. N. & KLEBANOFF, P. S. 1967 Higher-order correlations in a turbulent field. *Phys. Fluids* **10**, 507–520.

HANJALIĆ, K. & LAUNDER, B. E. 1972 A Reynolds stress model of turbulence and its application to thin shear flows. *J. Fluid Mech.* **52**, 609–638.

HISHIDA, M. & NAGANO, Y. 1978 Simultaneous measurements of velocity and temperature in nonisothermal flows. *Trans. ASME* C: *J. Heat Transfer* **100**, 340–345.

HISHIDA, M. & NAGANO, Y. 1979 Structure of turbulent velocity and temperature fluctuations in fully developed pipe flow. *Trans. ASME* C: *J. Heat Transfer* **101**, 15–22.

HISHIDA, M. & NAGANO, Y. 1981 Structure of pipe flow turbulence. Part 2. Coherent structures near the wall. *Trans. Japan Soc. Mech. Engrs* B **47**, 50–58.

HISHIDA, M., NAGANO, Y. & TAGAWA, M. 1986 Transport processes of heat and momentum in the wall region of turbulent pipe flow. In *Proc. 8th Intl Heat Transfer Conf.*, vol. 3, pp. 925–930. San Francisco.

KAMPÉ DE FÉRIET, J. 1966 *David Taylor Model Basin Rep. 2013.* Naval Ship Research and Development Center, Washington DC.

LU, S. S. & WILLMARTH, W. W. 1973 Measurements of the structure of the Reynolds stress in a turbulent boundary layer. *J. Fluid Mech.* **60**, 481–511.

LUMLEY, J. L. 1978 Computational modeling of turbulent flows. In *Advances in Applied Mechanics*, vol. 18 (ed. C.-S. Yih), pp. 123–176. Academic.

MONIN, A. S. & YAGLOM, A. M. 1971 *Statistical Fluid Mechanics*, vol. 1. MIT Press, Cambridge.

NAGANO, Y. & HISHIDA, M. 1985 Production and dissipation of turbulent velocity and temperature fluctuations in fully developed pipe flow. In *Proc. 5th Intl Symp. on Turbulent Shear Flows*, pp. 14.19–14.24. Cornell University.

NAGANO, Y. & TAGAWA, M. 1988 Coherent motions and their role in heat transport processes in a wall turbulent shear flow. *J. Fluid Mech.* (submitted).

NAKAGAWA, H. & NEZU, I. 1977 Prediction of the contributions to the Reynolds stress from bursting events in open-channel flows. *J. Fluid Mech.* **80**, 99–128.

OWEN, R. G. 1973 An analytical turbulent transport model applied to non-isothermal fully-developed duct flows. PhD Thesis, Pennsylvania State University.

PERRY, A. E. & HOFFMANN, P. H. 1976 An experimental study of turbulent convective heat transfer from a flat plate. *J. Fluid Mech.* **77**, 355–368.

SULLIVAN, P. J. & YIP, H. 1985 A solution-scheme for the convective-diffusion equation. *Z. angew. Math. Phys.* **36**, 596–608.

WYNGAARD, J. C. 1975 Modeling the planetary boundary layer: Extension to the stable case. *Boundary-Layer Met.* **9**, 441–460.

WYNGAARD, J. C. & COTÉ, O. R. 1974 The evolution of a convective planetary boundary layer: A Higher-order-closure model study. *Boundary-Layer Met.* **7**, 289–308.

ZARIĆ, Z. 1979 Statistical evidence on the phenomena in wall layers of turbulent flows. In *Turbulent Forced Convection in Channels and Bundles*, vol. 1 (ed. S. Kakaç & D. B. Spalding), pp. 377–401. Hemisphere.